Temperature dependence of magnetic excitations in the frustrated antiferromagnetic spinel $ZnMn_2O_4$

Hun Chang,[1] In-Yong Hwang,[1] Jae-Ho Chung,[1,*] J. Ross Stewart,[2] Wataru Higemoto,[3,4] and Yasuhiro Miyake[5]

[1]*Department of Physics, Korea University, Seoul 02841, South Korea*

[2]*ISIS Facility, Rutherford Appleton Laboratory, Harwell Oxford, Didcot, Oxfordshire OX11 0QX, United Kingdom*

[3]*Advanced Science Research Center, Japan Atomic Energy Agency, Tokai, Ibaraki 319-1195, Japan*

[4]*Department of Physics, Tokyo Institute of Technology, Meguro, Tokyo 152-0081, Japan*

[5]*High Energy Accelerator Research Organization (KEK), Tokai, Ibaraki 319-1106, Japan*

(Received 25 September 2017; revised manuscript received 24 November 2017; published 3 January 2018)

We report the temperature-dependent evolution of spin ordering and excitations of the frustrated tetragonal ($c > a$) spinel $ZnMn_2O_4$ across the two-dimensional antiferromagnetic transition. Muon spin relaxation indicates full development of ordered magnetic moments immediately below $T_N = 62.7(2)$ K in spite of the apparent low-dimensional ordering. Using inelastic neutron scattering, we obtained the spin Hamiltonian accounting for the temperature-dependent spin excitations. The damped spin waves at high temperature exhibit a continuous increase in their lifetime on cooling across T_N. In contrast, the finite anisotropy gap appears suddenly below T_N indicating that single-ion anisotropy stabilizes the antiferromagnetic chains. We also observed the frustrated out-of-plane exchange contributing to the high-energy modes.

DOI: 10.1103/PhysRevB.97.014406

I. INTRODUCTION

In antiferromagnetic materials, the establishment of long-range ordering is often hindered by the symmetries of underlying crystal structures. Such phenomena, or geometrical frustrations, are known to be strong in cubic spinel oxides (AB_2O_4) particularly when their nearest-neighbor B-B bonds compete among themselves to satisfy the antiferromagnetic exchanges. Long-range magnetic order is often achieved often via various lattice distortions breaking the degeneracy among six B-B bonds within the B_4 tetrahedra. Good examples of this are found in chromites, or ACr_2O_4 (A = Zn, Cd, Hg, Mg), where Cr^{3+} ions are subject to no orbital asymmetry [1–4]. In spite of the apparent similarities, these materials exhibit an interesting variety of magnetostructural distortions leading to complex magnetic order. Whereas a simple ordering is expected on uniaxial lattice contraction ($c < a$), $ZnCr_2O_4$ and $MgCr_2O_4$ in their tetragonal phases exhibit complex magnetic structures with multiple magnetic ordering wave vectors [5–8]. $CdCr_2O_4$, in contrast, establishes incommensurate magnetic order on tetragonal elongation ($c > a$), the origin of which is not well understood [9]. $HgCr_2O_4$ shows an even more complicated ground state involving an orthorhombic structure and multiple magnetic ordering vectors [10]. These observations commonly suggest that the geometrical frustrations continue to play a significant role in the distorted spinel lattices.

In this paper, we are particularly interested in the spinel oxides with tetragonal elongations along c axes ($c > a$) as depicted in Fig. 1(a). The prototypical example is found in manganites, or AMn_2O_4, where the elongation is robustly supported by strong Jahn-Teller effect of octahedral Mn^{3+} ($3d^4$: $t_{2g}^3 e_g^1$, $S = 2$) ions. When no additional orbital degeneracies are involved, the space group of the crystal lattice changes from cubic $Fd\bar{3}m$ to tetragonal $I4_1/amd$ causing the Mn-Mn bonds to become longer along the c axis. Since the direct exchanges between adjacent Mn^{3+} ions should be stronger along the bonds in the c planes (J_1), antiferromagnetic spin chains are expected to form in these planes. While one-dimensional chains will not be stable due to their propensity for thermal disorder, even in three dimensions their long-range orderings often turn out to be nontrivial. This is because the spin chains on any pair of adjacent planes are orthogonal to each other and thus the out-of-plane interchain exchanges (J_1') cancel out [for instance, see Fig. 1(c)]. It was suggested that the associated geometrical frustration should cause magnetostructural instabilities in Mn_3O_4 [11–13]. When the tetragonal symmetry remains intact, Mn_3O_4 shows the Yafet-Kittel-type ferrimagnetic ordering where tilting patterns of Mn^{3+} spins reverse between two parallel chains [14,15]. Such magnetic cell-doubling (CD) modulations propagate along the net magnetization direction parallel to the a axis, which are observed by neutron diffraction as magnetic Bragg peaks according to the ordering wave vector $\mathbf{k}_{CD} = (1/2, 1, 0)$ [11,12]. These CD peaks become suppressed when the underlying geometrical frustration is perturbed via orthorhombic distortions [16].

$ZnMn_2O_4$ apparently is one of the simplest among c-elongated tetragonal spinels as its tetrahedral A ions are nonmagnetic [17,18]. Although the Curie-Weiss temperature indicates strong antiferromagnetic interactions ($|\Theta_{CW}| \approx 900$ K), its magnetization data typically show weakly spin-glass behaviors without revealing clear transitions suggesting persistent geometrical frustration [19]. The transition to the long-range ordered antiferromagnetic phase has only recently been identified in heat capacity measurements ($T_N \approx 60$ K), below which the ordered phase involved the CD modulations similar

*jaehc@korea.ac.kr

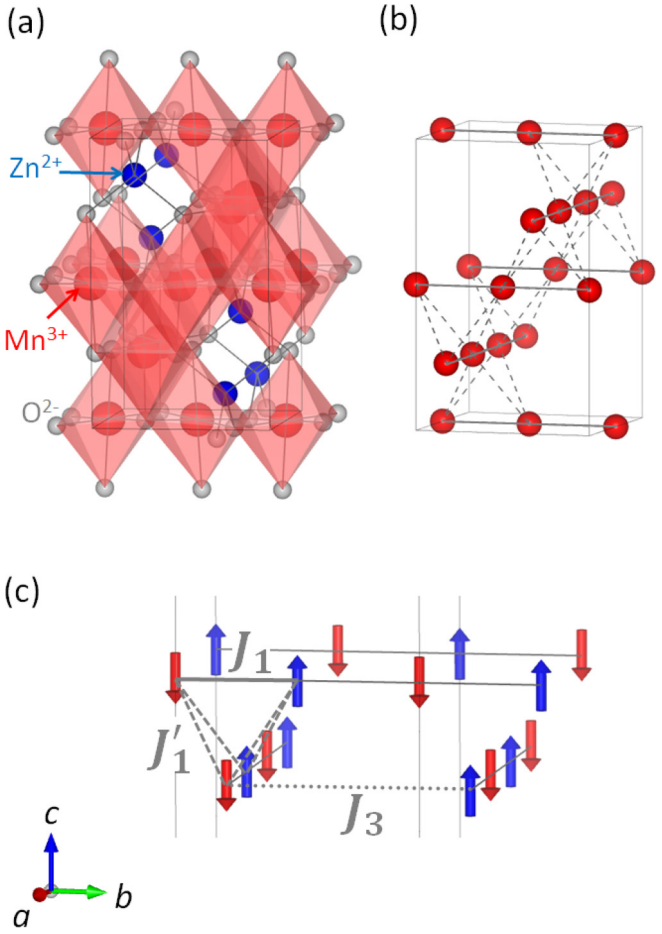

FIG. 1. (a) The crystal structure of $ZnMn_2O_4$ shown on its body-centered tetragonal unit cell. The shaded polyhedra represent octahedral oxygen cages enclosing Mn^{3+} ions. (b) The substructure of Mn^{3+} ions on the B sites of AB_2O_4 spinel. The solid and dashed lines connecting ions represent in-plane and out-of-plane bonds, respectively. (c) The antiferromagnetic spin arrangements on the Mn^{3+} sites exhibiting the cell-doubled ordering simultaneously along the a and b axes. Also shown are exchange constants included in the spin wave calculations discussed in the text.

to Mn_3O_4 [20]. Two-dimensional spin fluctuations were reported to develop via interchain antiferromagnetic exchanges at high temperatures followed by static ordering upon cooling below T_N. In our current work, we investigated the temperature-dependent evolution of magnetic order and excitations in $ZnMn_2O_4$ with a particular emphasis on how the long-range order becomes stabilized across T_N. By combining muon spin relaxation (μSR) and neutron scattering measurements on a polycrystalline sample, we find that the magnetic easy-axis anisotropy of Mn^{3+} ions plays a decisive role in stabilizing long-range antiferromagnetic order.

II. EXPERIMENTAL

The polycrystalline samples of $ZnMn_2O_4$ were synthesized by heating a mixture of ZnO and Mn_2O_3 at 1,323 K for 24 hours. Using x-ray powder diffraction, the obtained samples were confirmed to be single phase with the lattice parameters $a = 5.7163(1)$ Å and $c = 9.2520(1)$ Å at room temperature. Magnetic susceptibility was measured using vibrating sample magnetometry under an applied field of 1 kOe. Muon spin relaxation measurements were performed in zero field using the D1 (MUSE) instrument of KEK at J-PARC. Time-of-flight inelastic neutron scattering measurements were performed using the MARI spectrometer at the ISIS facility of the Rutherford Appleton Laboratory. We used neutron beams with two different incident energies, $E_i = 50$ and 150 meV, for obtaining high- and low-resolution data, respectively. The associated full-width-half-maxima in energy were adjusted by the chopper frequencies to be 1.60 meV and 5.81 meV, respectively.

III. RESULTS AND DISCUSSIONS

We begin by discussing the temperature dependence of zero-field μSR asymmetry, $A(t) = [F(t) - \alpha B(t)]/[F(t) + \alpha B(t)]$, obtained from polycrystalline $ZnMn_2O_4$. Above, $F(t)$ and $B(t)$ are positron counts in the forward and backward detectors, respectively, while α is the relative counting efficiency [21]. A time-dependent decrease of the muon asymmetry

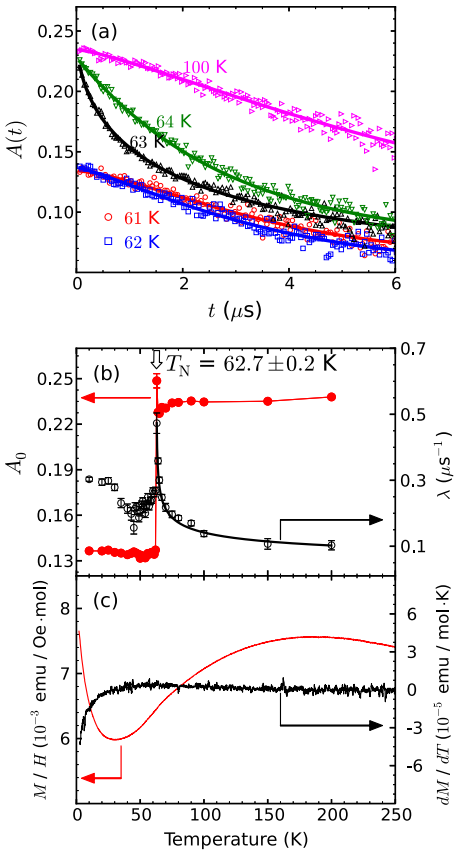

FIG. 2. (a) Time-dependent zero-field μSR asymmetries of polycrystalline $ZnMn_2O_4$ at selected temperatures. The plotted asymmetries include a few percent of contributions from a silver backing plate. The solid lines through the data are the stretched exponential fitting curves as discussed in the text. The obtained best-fit parameters, A_0 and λ, are shown in (b). The Néel temperature, T_N, was obtained by the inverse power-law fitting to $\lambda(T)$. (c) The temperature dependences of dc magnetic susceptibility and its temperature derivative under the external field $H = 1$ kOe.

generally indicates depolarization of spin-polarized μ^+ particles under the sample's local magnetic field. While the $A(t)$ curves showed almost linear decreases at high temperatures, significant curvatures developed as the temperature was lowered below 100 K as shown in Fig. 2(a). Such changes indicate that antiferromagnetic fluctuations preexisted at $T > 100$ K and slowed down near T_N reaching a time scale of a few μs. Nevertheless, the initial value of the asymmetry, $A(t = 0) \equiv A_0$, remained almost unchanged down to 63 K suggesting the lack of static magnetic ordering. The initial asymmetry finally dropped abruptly at 62 K indicating the local stabilizations of magnetic moments. The apparent absence of muon-spin precession at small t suggests that the depolarizations occur much faster than the time resolution of the current measurement ($\Delta t = 0.08\,\mu$s), which is not surprising given the expected large magnetic moment of Mn^{3+} ions ($\approx 4\mu_B$) [20]. We obtain the initial asymmetries by fitting a stretched exponential from, $A(t) = A_0 \exp[-(\lambda t)^\beta]$, and plot the temperature dependences of the obtained parameters in Fig. 2(b). The value of A_0 exhibits a sharp decrease near 63 K within a temperature range narrower than 1 K clearly indicating that static magnetic moments appear abruptly. The relaxation rate, $\lambda(T)$, consistently shows a sharp divergence, from which we estimated the Néel ordering temperature to be $T_N = 62.7(2)$ K. Below T_N, the relaxation rate rapidly decreases and then exhibits a weak enhancement below 40 K. Such behavior suggests that a significant degree of spin fluctuations persist in the long-range ordered phase of $ZnMn_2O_4$ [22–25].

The abrupt change in the μSR spectra is in striking contrast to the dc magnetization, $M(T)$, which is plotted in Fig. 2(c) for comparison. The latter only shows the smooth downturn that appears below 200 K and continues on cooling across T_N, finally reaching a minimum well below the ordering temperature. No relevant features are observed in dM/dT except the change of sign well below T_N. Such behavior of the dc magnetization is explained as the development of one- or two-dimensional antiferromagnetic spin correlations susceptible to thermal instabilities [26,27]. While such is consistent with the previously reported two-dimensional magnetic ordering [20], the changes observed in the μSR spectra are surprisingly sharp for the supposed low dimensionality. We suppose that additional interactions should contribute to the local stability of spins and make them appear static on the time scale of the muon response.

In order to understand magnetic interactions underlying the apparent low-dimensional ordering, we performed time-of-flight inelastic neutron scattering measurements over a wide temperature range below 300 K. We first used an incident energy of $E_i = 150$ meV in order to visualize the full excitation spectra. As displayed in the top panel of Fig. 3, the excitation spectra appeared to have similar patterns between 300 K and 45 K in spite of the large temperature difference. The intensities at higher momentum transfer ($Q \gtrsim 6$ Å^{-1}) and extending up to about 80 meV in energy transfer are ascribed to phonon excitations, whereas magnetic excitation intensities are limited to below 30 meV and 5 Å^{-1}. We thus selected an incident energy of $E_i = 50$ meV for further measurements.

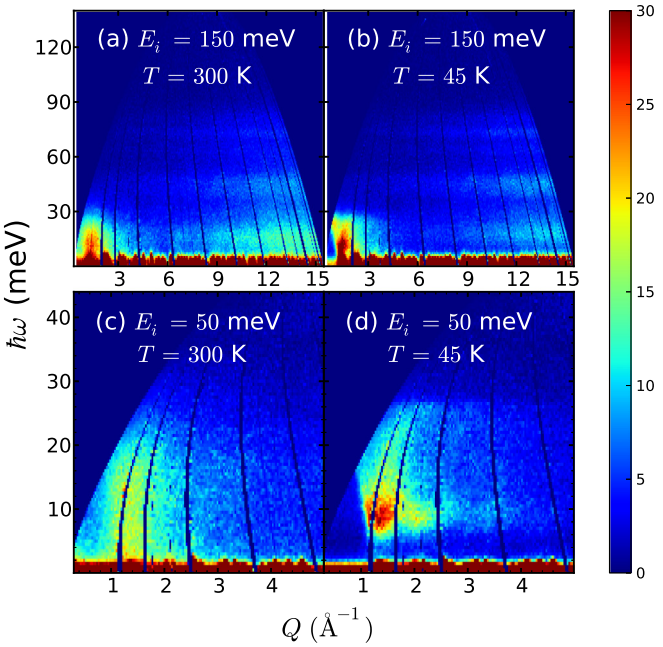

FIG. 3. Time-of-flight neutron scattering intensities of polycrystalline $ZnMn_2O_4$. The neutron energy incident to the sample is $E_i = 150$ meV for the top panel, and $E_i = 50$ meV for the bottom. The measurement temperatures, 300 K ($>T_N$) or 45 K ($<T_N$), are denoted in the corresponding plots. Dark curved areas extending upwards are due to the detector gaps of the instrument.

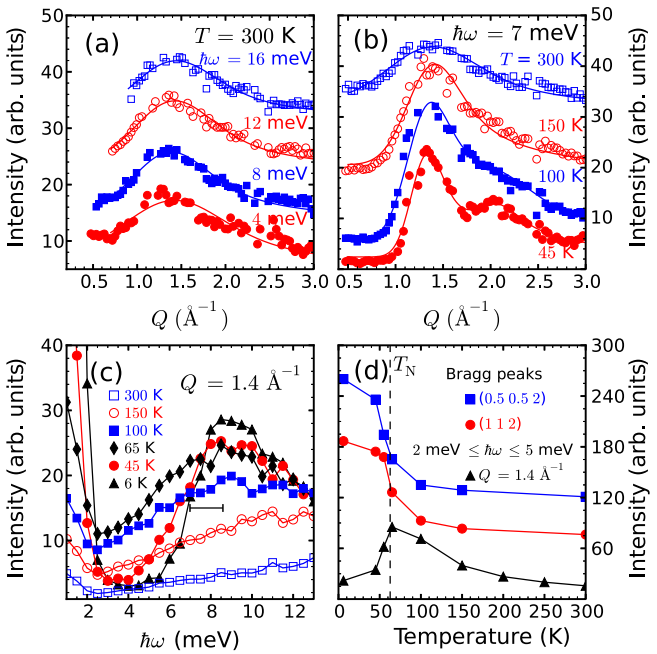

FIG. 4. Constant-$\hbar\omega$ cuts from the time-of-flight neutron scattering spectra for (a) selected energy transfers at 300 K and (b) selected temperatures at $\hbar\omega = 7$ meV. The solid lines through the data are fitting curves using asymmetric Warren line-shape functions [28]. (c) Constant-Q cuts ($Q = 1.4$ Å^{-1}) of the neutron scattering spectra at selected temperatures. The horizontal bar indicates the energy resolution at $\hbar\omega \approx 8$ meV. (d) Temperature dependencies of magnetic Bragg peak and low-energy inelastic scattering intensities. The vertical dashed line marks $T_N = 62.7$ K.

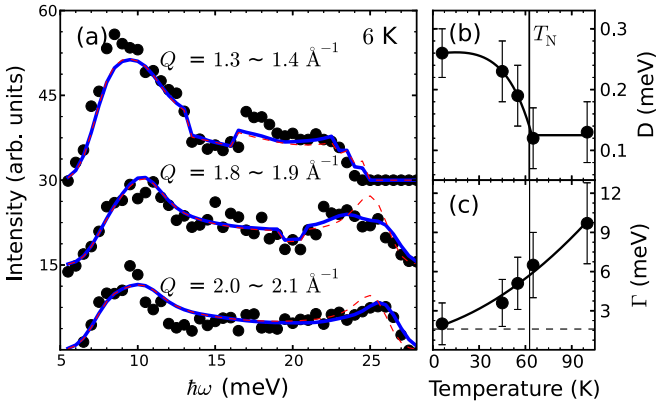

FIG. 5. (a) Inelastic neutron scattering intensities at 6 K integrated over finite Q ranges as shown in the panel. Solid lines are the calculated intensities using the model discussed in the text and the parameters listed in Table I. Dashed lines show the similar calculations with J_1' set to be zero for comparison. The sudden dips in the top two plots are ascribed to the missing detectors. Temperature dependences of (b) the single-ion anisotropy and (c) the full-width-half-maximum obtained from the least-square fitting method. Solid lines are guides to the eye. In (c), the horizontal dashed line marks the instrumental resolution of 1.60 meV.

As shown in Fig. 3(c), the magnetic excitation at 300 K showed a broad distribution in intensity centered around $Q = 1.4$ Å^{-1} and extending approximately up to $\hbar\omega = 27$ meV. The plots in Fig. 4(a) show that its momentum dependence is virtually independent of the energy transfer, which suggests that spin fluctuations are short ranged at this temperature. As the temperature was lowered toward T_N, the excitation spectra underwent significant changes particularly in their momentum dependence. As shown in Fig. 4(b), the excitation at 150 K looks significantly asymmetric in Q and can be fitted by the Warren line-shape function [28]. Such an asymmetric peak line shape is consistent with the previously observed development of extended two-dimensional spin correlations [20]. Finally, below T_N, typical spin-wave-like dispersions emerge with a finite anisotropy gap [see Fig. 3(d)]. Excitation intensities were accumulated strongly around ~9 meV reflecting the magnon states concentrated above the anisotropy gap, from which dispersive modes extend upward and sideways at the same time. We notice that the upper cutoff energy is virtually unchanged across the transition, which suggests that the disordered phase well above T_N already is subject to strong antiferromagnetic exchange interactions [19]. We also found that the low-energy excitation gap starts to develop immediately below T_N as shown in Fig. 4(c). The plots in Fig. 4(d) clearly show that such development of the gap is directly related to the stabilization of long-range antiferromagnetic ordering indicated by the magnetic Bragg peaks.

TABLE I. The exchange and anisotropy constants obtained at 6 K from the least-squares fitting of the inelastic neutron scattering intensities. The corresponding experimental and calculated spectra are shown in Figs. 5(a), 6, and 7(b).

S	J_1	J_1'	J_3	D
2	6.0(3) meV	0.6(5) meV	0.15(5) meV	0.26(4) meV

We performed the quantitative analysis of the observed magnetic excitation spectra using the linear spin-wave calculations in the Holstein-Primakoff formalism. First, we used the two-dimensional magnetic structure with the CD ordering suggested by Disseler *et al.* assuming that each Mn^{3+} spin

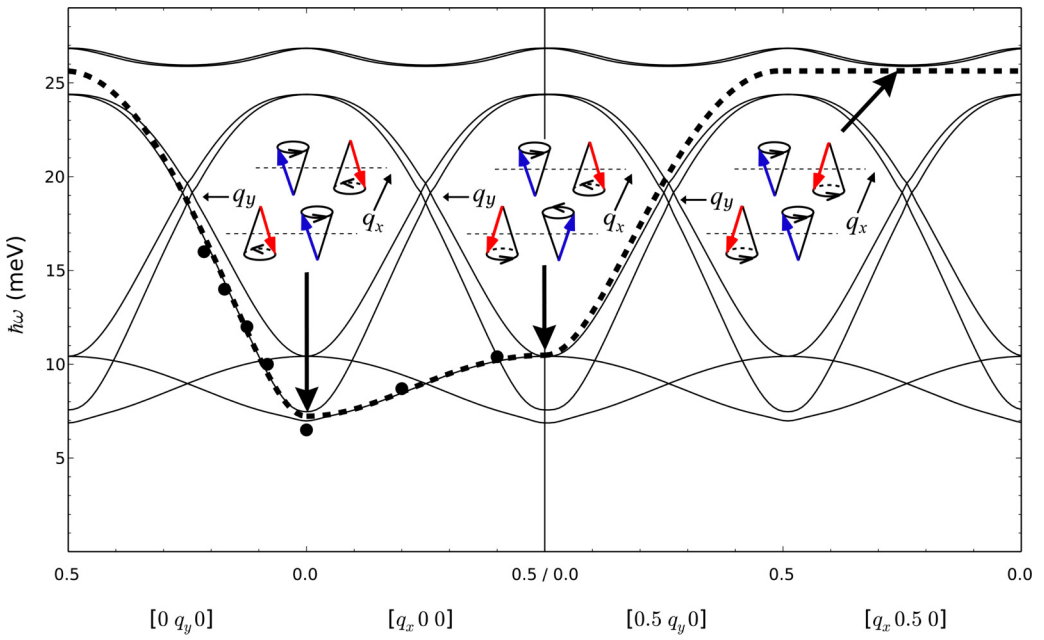

FIG. 6. Thin solid lines show the spin wave dispersions calculated as discussed in the text using the parameters listed in Table I. Thick dashed lines are calculated using Eq. (2) excluding J_1'. The insets illustrate the spin displacement patterns for the corresponding modes indicated by arrows. The filled circles on the left panel are the single-crystal data reproduced from Ref. [20].

($S = 2$) is oriented along the c axis [20]. The spin Hamiltonian includes the isotropic exchanges, J_{ij}, and the uniaxial single-ion anisotropy constant along the c axis, D, as below:

$$H = \frac{1}{2}\sum_{i,j} J_{ij}(\vec{S}_i \cdot \vec{S}_j) - \sum_i D(\vec{S} \cdot \hat{c})^2. \quad (1)$$

As illustrated in Fig. 1(c), we assigned J_1 for exchanges between the intrachain nearest-neighbor spins, and J_3 between interchain pairs to account for the CD ordering [20]. We then obtain the following analytical solution for the twofold degenerate modes:

$$\hbar\omega(q_x,q_y) = 2S\sqrt{(J_1+J_3+D)^2 - [J_3\cos(2q_x\pi) + J_1\cos(q_y\pi)]^2}. \quad (2)$$

The above solution is given as a function of the reduced in-plane wave vector $\vec{q} = (q_x,q_y,0)$ with respect to the magnetic ordering wave vector $\mathbf{k}_{\mathrm{CD}} = (1/2,1,0)$. Assuming that the intrachain exchange is significantly stronger than the interchain ($J_1 > J_3$), the solution gives the maximum magnon energy of $\hbar\omega(0,\frac{1}{2}) = 2S\sqrt{(J_1+J_3+D)^2 - J_3^2}$ along the intrachain mode. In comparison, the interchain mode will reach its maximum at the lower energy, $\hbar\omega(\frac{1}{2},0) = 2S\sqrt{(J_1+J_3+D)^2 - (J_3-J_1)^2}$, along the perpendicular direction in the reciprocal lattice.

In order to obtain quantitative values of the involved constants, we performed a least-squares fit of the calculated scattering cross sections to the experimental data. We first obtained the dynamical magnetic structure factor, $\vec{F}_{\mathrm{M}}(\omega,\vec{Q})$, from the linear spin waves, and subsequently calculated the inelastic neutron scattering cross sections using the single mode approximation as follows [29–32]:

$$I(\omega,\vec{Q}) \propto \frac{1}{\omega}|\hat{Q}\times\vec{F}_{\mathrm{M}}(\omega,\vec{Q})\times\hat{Q}|^2[n(\omega)+1], \quad (3)$$

where $n(\omega)$ is the Bose factor. The calculated cross sections were then convoluted by a Gaussian peak-shape function of the full-width-half-maximum, Γ, in energy transfer. The powder-averaging integration was performed using the Monkhorst-Pack algorithm [33], and the process was iterated to find the set of the best-fit parameters. Figure 5(a) shows the direct comparison between the experimental data at 6 K and the best-fit calculations (see the dashed lines) at several momentum transfers. The calculations using the current two-dimensional model reasonably reproduced the experimental data at low energies. However, significant disagreements were visible at high energies. Most importantly, the model calculation overestimated the intensity distribution near $\hbar\omega = 25$ meV [see the plot in the middle of Fig. 5(a)] and failed to account for weak dispersions nearby [see the bottom plot in Fig. 5(a)]. The best-fit parameters of J_1, J_3, and D, respectively, obtained from these calculations are listed in Table I [34]. The corresponding spin wave energies are shown in Fig. 6 as thick dashed lines along high-symmetry directions, which apparently reproduce the previous single-crystal data at low energies reasonably well [20].

From the analysis of the eigenvectors, we identify that the high-energy modes involve opposite motions of the nearest

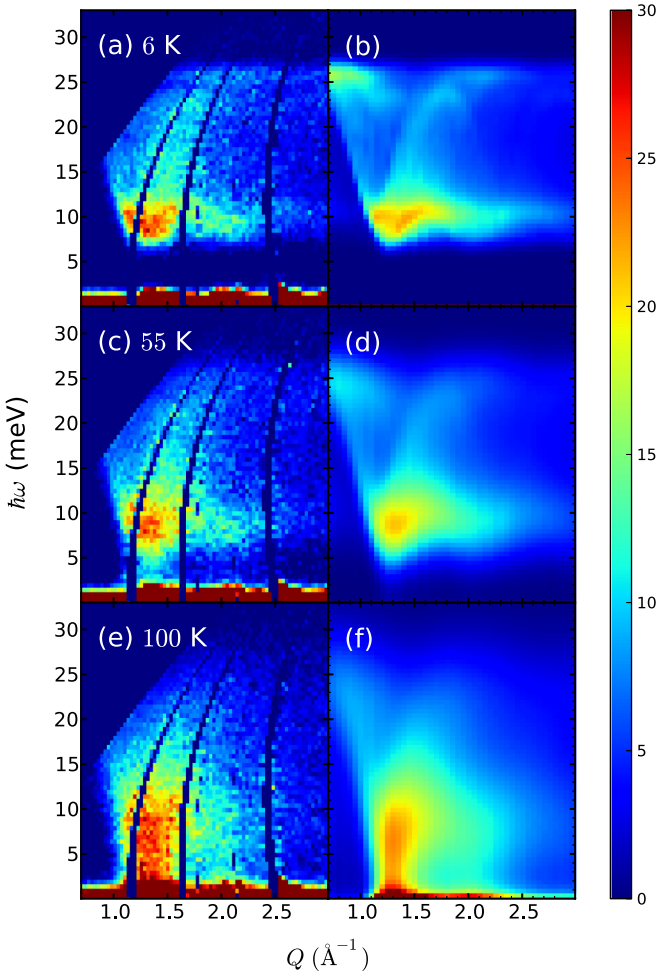

FIG. 7. The left panels show the time-of-flight inelastic neutron scattering intensities observed at selected temperatures, which were subtracted with constant-Q backgrounds. The right panels show the spin wave excitation intensities calculated at corresponding temperatures using the model including all parameters listed in Table I as well as Γ as discussed in the text. Only D and Γ were assumed to vary with temperature while the other parameters were fixed.

intrachain spin pairs (see the inset in Fig. 6). It suggests that they should be subject to the antiferromagnetic exchanges between two orthogonal spin chains at adjacent c planes, which should otherwise be frustrated. We therefore introduced an additional exchange constant, J_1', out of the c planes as depicted in Fig. 1(c). To accommodate it and account for the CD orderings simultaneously along a and b axes, we extended the magnetic supercell to include 16 spins in total. As shown with solid lines in Fig. 5(a), excellent agreement was achieved for the high-energy modes when we used $J_1' \approx 0.1J_1$. The associated dispersions are plotted as thin solid lines in Fig. 6, which reveal a gap appearing in the high-energy modes. Although the full analytical solutions are not available for this model, we find that the out-of-plane exchange causes the splitting by $\pm SJ_1'$ at the magnetic zone boundaries. The observed and calculated intensities at 6 K are also displayed as two-dimensional plots in Figs. 7(a) and 7(b), respectively, for comparison. Both of them commonly reveal weak discontinuities in intensity distribution near ~24 meV, which is caused by the presence of J_1'. These

results indicate that the geometrical frustration does not render the spin excitations in $ZnMn_2O_4$ to be truly two dimensional.

Finally, we investigated the quantitative changes in the inelastic excitation spectra as the temperature was increased across T_N. Since there are no structural phase transitions below 300 K, we assume the exchange interactions remain constant within the investigated temperature range. By adjusting only D and Γ as temperature-dependent parameters, we repeated the least-squares fitting of the inelastic neutron scattering intensities at higher temperatures. As shown in Fig. 7, the experimentally observed intensities could be well reproduced up to 100 K, at which point the excitation spectra exhibited significant broadening in line width and closing of the gap. We find that the single-ion anisotropy constant increases sharply near T_N as plotted in Fig. 5(b). In contrast, Fig. 5(c) shows that the line width decreases monotonously across T_N without noticeable anomalies. It indicates that the lifetime of the spin excitations increases monotonously suggesting a continuous stabilization of the spin wave modes across the antiferromagnetic transition. The comparison between two sets of data provides an explanation of the apparently contrasting temperature dependencies of the μSR asymmetry and dc magnetization. While the robustness of long-range order will directly determine spin wave lifetime as well as dc magnetization, the local stabilities due to single-ion anisotropy will primarily affect the μSR spectra. The simultaneous sharp changes observed in $A_0(T)$ and as well as in $D(T)$ can thus be viewed as indicators of the local stability of spins. Upon local tilting due to thermal fluctuations, the uniaxial anisotropy term $[-D(\vec{S}\cdot\hat{c})^2]$ will provide a better stability than isotropic exchanges of similar magnitudes. We thus conclude that the uniaxial single-ion anisotropy plays the most important role in stabilizing the antiferromagnetic ordering in $ZnMn_2O_4$.

IV. SUMMARY

We investigated the temperature-dependent dynamics in the frustrated tetragonal ($c > a$) spinel $ZnMn_2O_4$, where two-dimensional order of antiferromagnetic spin chains had been reported [20], While the transition to the ordered phase was not detected by dc magnetization, the zero-field μSR showed a clear and sharp transition at $T_N = 62.7(2)$ K. By performing linear spin wave analysis on the powder-averaged inelastic neutron scattering data, we obtained the spin Hamiltonian including the in-plane as well as frustrated out-of-plane exchanges that successfully accounted for the magnetic order and excitations below T_N. As the temperature is increased across T_N, the lifetime of the observed spin waves decreases monotonously contrary to the sharp change in the single-ion anisotropy. We thus conclude that the stability of the antiferromagnetic ordering in $ZnMn_2O_4$ is ascribed to the local magnetic anisotropy in competition with thermal instabilities of the long-range two-dimensional spin correlations.

ACKNOWLEDGMENTS

This research was supported by the Basic Science Research Program (NRF-2016R1D1A1B03934157) and the International Cooperation in S&T Program (NRF-2017K1A3A7A09016303) through the National Research Foundation of Korea (NRF).

[1] S.-H. Lee, C. Broholm, T. H. Kim, W. Ratcliff II, and S.-W. Cheong, Phys. Rev. Lett. **84**, 3718 (2000).
[2] J.-H. Chung, M. Matsuda, S.-H. Lee, K. Kakurai, H. Ueda, T. J. Sato, H. Takagi, K.-P. Hong, and S. Park, Phys. Rev. Lett. **95**, 247204 (2005).
[3] H. Ueda, H. Mitamura, T. Goto, and Y. Ueda, Phys. Rev. B **73**, 094415 (2006).
[4] H. Ehrenberg, M. Knapp, C. Baehtz, and S. Klemme, Powder Diffr. **17**, 230 (2002).
[5] O. Tchernyshyov, R. Moessner, and S. L. Sondhi, Phys. Rev. Lett. **88**, 067203 (2002).
[6] S. Ji, S.-H. Lee, C. Broholm, T. Y. Koo, W. Ratcliff, S.-W. Cheong, and P. Zschack, Phys. Rev. Lett. **103**, 037201 (2009).
[7] M. C. Kemei, P. T. Barton, S. L. Moffitt, M. W. Gaultois, J. A. Kurzman, R. Seshadri, M. R. Suchomel, and Y.-I. Kim, J. Phys.: Condens. Matter **25**, 326001 (2013).
[8] L. Ortega-San-Martín, A. J. Williams, C. D. Gordon, S. Klemme, and J. P. Attfield, J. Phys.: Condens. Matter **20**, 104238 (2008).
[9] J.-H. Chung, Y. S. Song, S. Park, H. Ueda, Y. Ueda, and S.-H. Lee, J. Korean Phys. Soc. **62**, 1900 (2013).
[10] M. Matsuda, H. Ueda, A. Kikkawa, Y. Tanaka, K. Katsumata, Y. Narumi, T. Inami, Y. Ueda, and S.-H. Lee, Nature Phys. **3**, 397 (2007).
[11] J.-H. Chung, K. H. Lee, Y.-S. Song, T. Suzuki, and T. Katsufuji, J. Phys. Soc. Jpn. **82**, 034707 (2013).
[12] Y. Nii, H. Sagayama, H. Umetsu, N. Abe, K. Taniguchi, and T. Arima, Phys. Rev. B **87**, 195115 (2013).
[13] M. C. Kemei, J. K. Harada, R. Seshadri, and M. R. Suchomel, Phys. Rev. B **90**, 064418 (2014).
[14] Y. Yafet and C. Kittel, Phys. Rev. **87**, 290 (1952).
[15] G. B. Jensen and O. V. Nielsen, J. Phys. C **7**, 409 (1974).
[16] K. H. Lee, H. Chang, I. Y. Hwang, J.-H. Chung, H. W. Kang, S. J. Kim, and S. Lee, Phys. Rev. B **91**, 064404 (2015).
[17] K. S. Irani, A. P. B. Sinha, and A. B. Biswas, J. Phys. Chem. Solids **23**, 711 (1962).
[18] Y. Aiyama, J. Phys. Soc. Jpn. **21**, 1684 (1966).
[19] D. P. Shoemaker, E. E. Rodriguez, R. Seshadri, I. S. Abumohor, and T. Proffen, Phys. Rev. B **80**, 144422 (2009).
[20] S. M. Disseler, Y. Chen, S. Yeo, G. Gasparovic, P. M. B. Piccoli, A. J. Schultz, Y. Qiu, Q. Huang, S.-W. Cheong, and W. Ratcliff II, Sci. Rep. **5**, 17771 (2015).
[21] S. J. Blundell, Contemp. Phys. **40**, 175 (1999).
[22] V. S. Zapf, B. G. Ueland, M. Laver, M. Lonsky, M. Pohlit, J. Müller, T. Lancaster, J. S. Möller, S. J. Blundell, J. Singleton, J. Mira, S. Yañez-Vilar, and M. A. Señarís-Rodríguez, Phys. Rev. B **93**, 134431 (2016).
[23] P. Carretta, M. Filibian, R. Nath, C. Geibel, and P. J. C. King, Phys. Rev. B **79**, 224432 (2009).
[24] A. Yaouanc, P. Dalmas de Réotier, P. C. M. Gubbens, A. M. Mulders, F. E. Kayzel, and J. J. M. Franse, Phys. Rev. B **53**, 350 (1996).

[25] M. T. Rovers, P. P. Kyriakou, H. A. Dabkowska, G. M. Luke, M. I. Larkin, and A. T. Savici, Phys. Rev. B **66**, 174434 (2002).
[26] M. E. Fisher, Am. J. Phys. **32**, 343 (1964).
[27] A. Seidel, C. A. Marianetti, F. C. Chou, G. Ceder, and P. A. Lee, Phys. Rev. B **67**, 020405(R) (2003).
[28] B. E. Warren, Phys. Rev. **59**, 693 (1941).
[29] S. M. Girvin, A. H. MacDonald, and P. M. Platzman, Phys. Rev. Lett. **54**, 581 (1985).
[30] G. Xu, J. F. DiTusa, T. Ito, K. Oka, H. Takagi, C. Broholm, and G. Aeppli, Phys. Rev. B **54**, R6827(R) (1996).
[31] S.-H. Lee, D. Louca, H. Ueda, S. Park, T. J. Sato, M. Isobe, Y. Ueda, S. Rosenkranz, P. Zschack, J. Íñiguez, Y. Qiu, and R. Osborn, Phys. Rev. Lett. **93**, 156407 (2004).
[32] V. O. Garlea, R. Jin, D. Mandrus, B. Roessli, Q. Huang, M. Miller, A. J. Schultz, and S. E. Nagler, Phys. Rev. Lett. **100**, 066404 (2008).
[33] H. J. Monkhorst and J. D. Pack, Phys. Rev. B **13**, 5188 (1976).
[34] We obtained the ratio $D/J_1 = 0.043$, which is an order of magnitude larger than $D/J_1 = 0.0032$ in Ref. [20].